

Detecting Radio Afterglows of Gamma-Ray Bursts with FAST *

Zhi-Bin Zhang¹, Si-Wei Kong², Yong-Feng Huang³, Di Li⁴, Long-Biao Li¹

¹ Department of Physics, College of Sciences, Guizhou University, Guiyang 550025, China;
sci.zbzhang@gzu.edu.cn

² Key Laboratory for Particle Astrophysics, Institute of High Energy Physics, Chinese Academy of Sciences, 19B Yuquan Road, Beijing 100049, China

³ Department of Astronomy, Nanjing University, Nanjing 210093, China; *hyf@nju.edu.cn*

⁴ National Astronomical Observatories of China, Chinese Academy of Sciences, 20A Datun Road, Beijing 100020, China

Received 2012 June 12; accepted 2012 July 27

Abstract Using the generic hydrodynamic model of Gamma-Ray Burst (GRB) afterglows, we calculate the radio afterglow light curves of low luminosity, high luminosity, failed and standard GRBs in different observational bands of FAST's energy window. The GRBs are assumed to be located at different distances from us. Our results show that the possibilities of detecting GRB radio afterglows decrease in order for high luminosity, standard, failed and low luminosity GRBs correspondingly. We predict that almost all types of radio afterglows except that of low luminosity GRBs could be observed by the worldwide largest radio telescope as long as the domains of time and frequency are appropriate. It is important to note that FAST can detect relatively weak radio afterglows at a higher frequency of 2.5 GHz for very high redshift up to $z=15$ or even more. Radio afterglows of low luminosity GRBs can be detected only if FAST is available in its second phase. We expect that FAST will largely expand the current sample of GRB radio afterglows in the near future.

Key words: gamma rays: bursts –methods: numerical–telescopes

1 INTRODUCTION

With prompt developments of space and ground telescopes, studies of Gamma-Ray Bursts (GRBs) have come into an era of full wavelengths (e.g. Gehrels & Razzaque 2013). Particularly, recent space missions such as Swift satellites, whose rapid response together with accurate localization enables more detailed follow-up observations by the ground facilities at longer times and lower frequencies, had led to deeper understanding of the physical origins of GRBs. In addition, statistical analysis becomes possible and more

and more important for comparing the properties of GRBs and their afterglows (Sakamoto et al. 2011). Prompt γ -rays and their follow-up X-ray and Optical afterglows are found to be correlated with each other, more or less, for both short and long-duration bursts (Gehrels et al. 2008; Nysewander et al. 2009; Kann et al. 2011). It was interesting that Chandra & Frail (2012) found the detectability of radio afterglows is only correlated with the optical brightness, but has no clear correlation with either the γ -ray fluences or the X-ray fluxes in statistics. However, observational investigations of radio afterglows are relatively poor, although some authors have recently compiled larger datasets (Postigo, 2012; Chandra & Frail 2012; Ghirlanda et al. 2013; Staley et al. 2013) since the first radio afterglow of GRB 970508 was discovered (Frail et al. 1997). To give a comparative study, we need to analyse the GRBs and their afterglows at a given energy band separately and then combine them to explore their comprehensive physics.

In the framework of the fireball internal-external shock model, GRBs are produced when the kinetic energy of an ultra-relativistic flow is dissipated by internal collisions, while the afterglows are emitted when the flow is slowed down by external shocks with the surrounding matter of the burst. The fireball model has given numerous successful predictions on GRB afterglows, such as the afterglow itself, jet break in the light curve of afterglows, the optical flash and the afterglow shallow-decay phenomena, etc. (e.g., see Lu et al. 2004, Piran 2004, Zhang 2007 for a review). Huang et al. (1999, 2000b) proposed a set of simplified dynamical equations that can consort with the self-similar solution of Blandford & McKee (1976) in the ultra-relativistic phase, and also consort with the Sedov solution (Sedov 1969) in the non-relativistic phase. Therefore, these equations can conveniently describe GRB afterglows at all the post-burst times. For instance, the beaming effects (Rhoads 1997, 1999; Huang, Dai & Lu 2000c), the rebrightening at multiple-wavelengths (Huang et al. 2004; Xu & Huang 2010; Kong, Wong, Huang & Cheng 2010; Yu & Huang 2013) and the multi-band afterglow modeling (Huang, Dai & Lu 2000c; Huang, Dai & Lu 2002; Huang & Cheng 2003; Wang, Huang & Kong 2009; Kong, Huang, Cheng & Lu 2009) can be easily dealt with by using those equations.

Square Kilometer Array (SKA) will be the largest and most sensitive radio telescope group in the world. The SKA project is designed to be constructed via two phases and will receive radio signals at a frequency range from 70 MHz to 10 GHz. As the largest worldwide single-dish radio telescope, Five-hundred-meter Aperture Spherical radio Telescope (FAST) is a Chinese megascience project that will be built in Guizhou province of southwest China by 2016. The FAST as the precursor of SKA covers radio frequencies of 70 MHz-3 GHz. It can be extended to 8 GHz in the second phase of SKA. The FAST will be equipped with a variety of instruments and has been designed for different scientific purposes including the radio afterglows of GRBs. According to the current data sets presented by Chandra & Frail (2012), the detection rate of radio afterglows is 30 %, in which more than half of the radio flux measurements are made at 8.5 GHz. However, nearly 10 percentage of the detected radio afterglows are from bright long GRBs (Ghirland et al. 2013; Salvaterra et al. 2012). The reason is that the low-frequency observations could be more affected by the bias of receivers.

In this work, we apply the fireball model to calculate a variety of numerical afterglow curves with changing redshifts for different cases representing failed, low luminosity, high luminosity and standard

compared with FAST's sensitivity in order to diagnose the detectability of the FAST. Our radio light curves within the FAST's window are derived for both low (70 MHz-0.5 GHz) and medium/high frequencies (0.5-3 GHz). The structure of our paper is as follows. Firstly, we introduce the theoretically dynamical model in Section 2 and the sensitivity of FAST in Section 3. Our numerical results are presented in Section 4. We briefly summarize and discuss our main results in Section 5.

2 DYNAMICAL MODEL

In terms of the generic dynamical model (Huang, Dai & Lu 1999, 2000a, 2000c), the overall evolution of the ejected outflows in either ultra-relativistic or non-relativistic (Newtonian) phase can be generally described as

$$\frac{dR}{dt} = \beta c \gamma (\gamma + \sqrt{\gamma^2 - 1}), \quad (1)$$

$$\frac{dm}{dR} = 2\pi(1 - \cos\theta)R^2 n m_p, \quad (2)$$

$$\frac{d\theta}{dt} = \frac{c_s}{R}(\gamma + \sqrt{\gamma^2 - 1}), \quad (3)$$

$$\frac{d\gamma}{dm} = -\frac{\gamma^2 - 1}{M_{ej} + \varepsilon m + 2(1 - \varepsilon)\gamma m}, \quad (4)$$

where R is the radial distance measured in the source frame from the initiation point; m is the rest mass of the swept-up circumburst medium; θ is the half-opening angle of the ejecta; γ is the bulk Lorentz factor of the moving material; t is the arrival time of photons measured in the observer frame; $\beta = \sqrt{1 - \gamma^{-2}}$, c is the speed of light. n is the number density of Interstellar Medium; ε is the general radiative efficiency and would evolve from 1 (high radiative case) to 0 (adiabatic case) within several hours after a burst; M_{ej} is the initial rest mass of the ejecta. c_s is the comoving sound speed determined by $c_s^2 = \hat{\gamma}(\hat{\gamma} - 1)(\gamma - 1)c^2/[1 + \hat{\gamma}(\gamma - 1)]$ with the adiabatic index $\hat{\gamma} = 4/3$ in the ultra-relativistic limit and $\hat{\gamma} = 1$ in the Newtonian limit (Huang et al. 2000b). We further define ξ_e and ξ_B^2 as the energy equipartition factors for electrons and the comoving magnetic field, respectively.

Denoting Θ as the viewing angle ($\equiv \theta_{obs}$) between the velocity of ejecta and the line of sight and $\mu = \cos\Theta$, in the burst comoving frame, we can obtain synchrotron radiation power of electrons at frequency ν' as (Rybicki & Lightman 1979)

$$P'(\nu') = \frac{\sqrt{3}e^3 B'}{m_e c^2} \int_{\min(\gamma_{e,min}, \gamma_c)}^{\gamma_{e,max}} \left(\frac{dN'_e}{d\gamma_e}\right) F\left(\frac{\nu'}{\nu'_c}\right) d\gamma_e, \quad (5)$$

in which $dN'_e/d\gamma_e \propto (\gamma_e - 1)^{-p}$ with the typical value of the electron distribution index p between 2 and 3 (Huang & Cheng 2003); $\nu'_c = 3\gamma_e^2 e B' (4\pi m_e c)^{-1}$ is the characteristic frequency of electrons with charge e ; $\gamma_c = 6\pi m_e c / (\sigma_T \gamma B'^2 t)$ is the typical Lorentz factor of electrons which cool rapidly due to synchrotron radiation with σ_T being the Thompson cross-section; $\gamma_{e,min} = \xi_e(\gamma - 1)m_p(p - 2)/[m_e(p - 1)] + 1$ and $\gamma_{e,max} \simeq 10^8 (B'/1G)^{-1/2}$ are respectively the minimum and the maximum of Lorentz factors of electrons, and $F(x) = x \int_x^{+\infty} K_{5/3}(x') dx'$ of which $K_{5/3}(x')$ is Bessel function. Owing to cosmological expansion, the observed frequency ν should be (Wang, Huang & Kong 2009)

here $\delta = [\gamma(1 - \beta\mu)]^{-1}$ is the Doppler factor. For low-frequency radiation, the effect of synchrotron self-absorption on observation should be considered and hence the observed flux density radiated from a cosmological point source would be (Huang et al. 2000b; Wang, Huang & Kong 2009)

$$F_\nu(t) = \frac{(1+z)\delta^3}{4\pi D_L^2} f(\tau) P'[(1+z)\nu/\delta], \quad (7)$$

where D_L is the luminosity distance and $f(\tau) = (1 - e^{-\tau_{\nu'}})/\tau_{\nu'}$ is a reduction factor of synchrotron self-absorption with an optical depth $\tau_{\nu'}$. In order to calculate the total observed flux densities, we should integrate Eq. (7) over the equal arrival time surface determined by

$$t = (1+z) \int \frac{1 - \beta\mu}{\beta c} = const, \quad (8)$$

within the jet boundaries.

3 FAST'S SENSITIVITY

In general, the sensitivity of an observation in radio astronomy is determined by the increase in the power level at the receiver input which causes a change in the output equaling the RMS noise. The output of the receiver detector is a function of the total power at the input of the receiver. The total input power consists of the target signal power and the extra noise power (e.g., thermal radiation and receiver noise). In Table 1, we list the values of sensitivity for different wavelengths for FAST. More detailed properties of FAST can refer to Nan et al. (2011).

The system temperature T_{sys} is the sum of T_A , the antenna noise temperature which results from the cosmic emission, the Earth's atmosphere and radiation from the Earth, and T_R , the receiver noise temperature, namely

$$T_{sys} = T_A + T_R. \quad (9)$$

Normally when observing cosmic sources, we can ignore T_A relative to T_{sys} and get the fluctuation of systematic noise as

$$\Delta T = \left[\frac{T_A^2 + T_A T_{sys} + T_{sys}^2}{\Delta\tau\Delta\nu} \right]^{1/2} \sim \frac{T_{sys}}{\sqrt{\Delta\tau\Delta\nu}}, \quad (10)$$

where $\Delta\tau$ and $\Delta\nu$ are respectively the bandwidth and the integral time. The smallest observable temperature of the systematic noise, i.e. RMS, can be estimated to be

$$\sigma = T_{A,min} = \Delta T_A \simeq \frac{T_{sys}}{\sqrt{\Delta\tau\Delta\nu}}. \quad (11)$$

The Signal Noise Ratio (SNR) is defined by

$$SNR = \frac{T_A}{\Delta T_A} = \frac{T_A}{T_{sys}} \sqrt{\Delta\tau\Delta\nu}. \quad (12)$$

The antenna temperature T_A and the output power F are related with

$$K_b T_A = \frac{A_e F}{2}. \quad (13)$$

The System Equivalent Flux Density (SEFD) can be calculated by

$$SEFD = \frac{F}{T_{sys}} = \frac{2K_b T_A}{T_{sys}} \quad (14)$$

Table 1 Parameters of the Nine Sets of FAST's Receivers

No.	Bands [†] GHz	ν_c^\dagger GHz	$\Delta\nu^\dagger$ MHz	T_{sys}^\dagger K	$F_{lim,1}$ μJy	$F_{lim,2}$ μJy	$F_{lim,3}$ μJy	T'_{sys} K	$F'_{lim,1}$ μJy	$F'_{lim,2}$ μJy	$F'_{lim,3}$ μJy
1	0.07-0.14	0.1	70	1000	293.6	168.7	119.4	140	41.0	23.5	16.9
2	0.14-0.28	0.2	140	400	82.5	47.6	33.8	140	28.8	16.6	11.9
3	0.28-0.56	0.4	280	150	21.9	12.7	8.9	130	19.1	11.1	7.8
4	0.56-1.02	0.8	560	60	6.1	3.6	2.5	97	9.9	5.8	4.2
5	0.32-0.334	0.328	14	200	130.7	75.3	53.5	125	81.7	47.1	33.2
6	0.55-0.64	0.6	90	60	15.5	8.9	6.4	112	28.9	16.6	11.9
7	1.15-1.72	1.45	550	25	2.5	1.4	1.1	61	6.3	3.6	2.5
8	1.23-1.53	1.38	300	25	3.6	1.9	1.4	60	8.6	5.0	3.6
9	2.00-3.00	2.5	1000	25	1.9	1.1	0.8	30	2.2	1.4	0.8

Notes: [†] These data are taken from Nan et al. (2011). $F_{lim,i}$ ($i=1, 2, 3$) denotes the limited flux densities for different integral time $\Delta\tau$ equaling 10, 30 and 60 minutes for the FAST's systematic temperatures. The limited flux densities $F'_{lim,i}$ ($i=1, 2, 3$) are estimated in terms of the system temperatures of the VLA's template within the above corresponding time levels.

where A_e is the effective area obtained by $A_e = \eta_A A_g$ with an aperture efficiency $\eta_A = 0.65$ (Yue et al. 2013) and the illuminated geometric area $A_g = \pi \times (300/2)^2 \text{ m}^2$ for the FAST (Nan et al. 2011). The RMS flux-density of radio receivers is

$$F_{lim} = \frac{2K_b T_{A,min}}{A_e} = \frac{2K_b T_{sys}}{A_e \sqrt{\Delta\tau \Delta\nu}} = \frac{SEFD}{\sqrt{\Delta\tau \Delta\nu}}. \quad (15)$$

4 RESULTS

To determine the sensitivity of FAST to GRB radio afterglows, we have chosen the failed, low-luminosity, high-luminosity and standard GRBs for a comparative study. For convenience, let us define the initial values or parameters of these bursts as follows. (1) Standard GRBs: initial isotropic energy $E_0 = 10^{52}$ ergs and $\gamma_0 = 300$; (2) High luminosity GRBs: initial isotropic energy $E_0 = 10^{54}$ ergs and $\gamma_0 = 300$; (3) Low luminosity GRBs: initial isotropic energy $E_0 = 10^{49}$ ergs and $\gamma_0 = 300$; (4) Failed GRBs: initial isotropic energy $E_0 = 10^{52}$ ergs and $\gamma_0 = 30$. Apart from these differences, we assume all the bursts have the same values for other parameters, namely $n = 1 \text{ cm}^{-3}$, $p = 2.5$, $\xi_e = 0.1$, $\xi_B^2 = 0.001$, $\theta = 0.1$ and $\Theta = 0$ throughout this paper. Also, an assumption of the radiative efficiency $\varepsilon = 0$ has been made because the relativistic fireball becomes fully adiabatic in about several hours after a burst. Light-curves of radio afterglows at different redshifts, i.e. $z=0.5, 1, 5, 10, 15$, have been derived in order to study FAST's capability of deep space observation for different kinds of bursts.

4.1 Light-Curves of Radio Afterglows in the FAST's Window

Figs. 1-5 show that almost all radio afterglow light curves, except the failed GRB afterglows exhibiting a bit difference, evolve with a similar profile of slow rise and fast decay (SRFD) although they may have distinct physical origins. We also find a common and interesting phenomenon that with the increase of observing frequency, the light curve peaks earlier, and the peak flux is also higher. At the same time, radio afterglows

to their similar kinetic energy. The two kinds of bursts decay congruously after their peak times. At higher frequencies and larger redshifts, the peak flux densities of failed GRBs are slightly weaker than those of the standard ones. This phenomenology indicates that both the peak flux density and the peak time of radio afterglows sensitively depend on the initial energy injection. For the failed GRBs, the rising part is largely affected by the small initial Lorentz factors of the ejecta from the central engine. In any cases, we notice that radio afterglows of the low luminosity GRBs have the lowest brightness except that they are stronger than those of the failed GRBs at early stage of less than 1hr. The intersection point would be postponed if the observing frequency is relatively lower for a farther burst. Note that it seems unlikely for FAST to detect any kinds of radio afterglow emission at the extremely lower frequency of ≤ 0.1 GHz. For bursts at the same distance or redshift, their radio flux density in higher frequency is usually stronger than that in lower frequency when they are observed at the same time and could be detected at a very early stage. Furthermore, it is found that the radio flux densities are relatively insensitive to the redshift as seen in Figs 3-5, which is in well agreement with some previous conclusions (e.g. Ciardi & Loeb 2000; Gou et al. 2004; Frail et al. 2006; Chandra & Frail 2012).

4.1.1 Standard GRBs

The thick solid lines in Figs. 1-5 denote the case of a standard fireball in different energy bands and redshifts. For the redshift $z = 0.5$, the peaked radio emissions at $\nu > 0.4$ GHz can be easily received by FAST. With the increase of observing frequency, the bursts gradually brighten. FAST can even detect very early radio afterglows in the prompt phase for a time of less than 10 second at 2.5 GHz. It is interesting that in high frequency bands, the radio afterglow can typically be observable for ~ 115 days. The peak flux densities at 1.4 GHz and 2.5 GHz can reach $70 \mu\text{Jy}$ and $200 \mu\text{Jy}$, respectively. For the redshift $z = 1$, FAST can detect the radio emission in the frequency band of $\nu > 0.6$ GHz, especially $\nu = 2.5$ GHz from 20 seconds to 62 days since a burst for 1 hour integration time. The earliest detection time may start as early as 10 seconds. For the redshift $z = 5$, radio afterglows under 0.8 GHz are undetectable for FAST. The peak flux densities at 0.8 GHz and 2.5 GHz can respectively reach $3 \mu\text{Jy}$ and $6 \mu\text{Jy}$, which will be observed up to 52 days from the earliest starting time of 30 minutes. For much higher redshifts of $z = 10$ and 15 , the radio flux densities have a peak value of $\sim 2 \mu\text{Jy}$ and only radio afterglows above 1.4 GHz can be marginally detected. Note that the GRB radio afterglows in the standard case usually peak at 10-100 days, which is well consistent with the observations described in Chandra & Frail (2012).

4.1.2 High Luminosity GRBs

The high luminosity GRBs marked with thick dashed lines in Figs. 1-5 are driven by the largest energy ejection and their radio afterglows naturally hold the strongest brightness when they are located at the same distance. For nearby bursts with a redshift of $z = 0.5$, FAST has the capability of detecting all radio afterglows at a frequency of no less than 100 MHz. The typical peak flux densities are $100 \mu\text{Jy}$ at 0.2 GHz and $7 \times 10^3 \mu\text{Jy}$ at 2.5 GHz respectively. The former can be detected from 3 days to 3.5 years and the later can be observed from several seconds to 9 years after the burst. For a redshift $z = 1$, FAST may detect the

6 years in a frequency of $\nu = 1.4$ GHz. The radio afterglow flux densities for redshift higher than 5 are undetectable under $\nu \simeq 300$ MHz and can be safely detected from 1 day to 2.5 years at 0.4 GHz and from several tens seconds to 4 years in high frequency bands. The peak radio flux densities in 0.4 -2.5 GHz for $z = 15$ can reach 50-200 μJy which is much higher than the threshold of FAST.

4.1.3 Low Luminosity GRBs

In contrast, the low luminosity GRBs denoted by dash-dot-dot lines in Figs.1-5 consist of some special bursts with lower energy input. This leads to smaller kinetic energy of outflows and then much weaker radio afterglows peaking at earlier time around 1 day after the GRB trigger. The weakest radio brightness is only $\sim 10^{-4} \mu\text{Jy}$ at 100 MHz for redshift $z = 15$. The strongest flux density can approach $0.3 \mu\text{Jy}$ at 2.5 GHz for $z = 0.5$ and is just close to the detection limit of FAST for 1 hour integration time. It is obvious that FAST can hardly detect radio afterglows from these low luminosity GRBs. In the future, if FAST's passband can be expanded to 8 GHz, then low luminosity GRBs may also be detected. We can also consider to increase the integration time to search low luminosity GRBs.

4.1.4 Failed GRBs

Such kinds of bursts are thought to be produced by an isotropic fireball with kinetic energy like that of the standard bursts but with much lower Lorentz factors of several tens. As shown in Figs. 1-5, radio afterglows of failed GRBs and the standard ones nearly peak simultaneously and they decay with time in the same way after the peak time. Compared with standard bursts, radio afterglows of failed bursts can be detected mainly at later times. For $z = 0.5$, FAST can hardly detect them at a frequency lower than 0.6 GHz in $3\text{-}\sigma$ levels with 1 hour integration time. But, we can detect the radio afterglows up to 85 days at higher frequency of 0.8 GHz. The afterglow is observable from a time of 1000 minutes, 70 minutes, 20 minutes, 15 minutes and 8 minutes for 0.6 GHz, 0.8 GHz, 1.38 GHz, 1.45 GHz and 2.5 GHz after the burst, respectively. For the redshift $z=1$, only radio emissions at a frequency larger than 0.6 GHz are detectable from 1 day to 60 days. Radio afterglow at a redshift $z = 5$ for a frequency larger than 1.4 GHz can be observed. The radio flux densities at 0.8 GHz, 1.38 GHz, 1.45 GHz and 2.5 GHz are in a lower level of 1-2 μJy . For $z > 10$, radio afterglows of the failed GRBs become very difficult to be detected by FAST with its current sensitivity of 1 hour integration time.

4.2 Peak Spectra of Radio Afterglows in the FAST's Window

To investigate the sensitivity of FAST's receiver at different frequencies, we plot the peak frequency against the peak flux density for the above-mentioned four types of bursts at different redshifts in Fig. 6. The data utilized here are extracted from the above calculations. Radio emission would be steeply cut off by the self-absorption effect at lower frequencies below several GHz. This frequency range covers the FAST's frequency bands of 70 MHz-3 GHz, which causes the radio flux density F to be a power-law function of $F \propto \nu^2$ (e.g. Sari, Piran & Narayan 1998; Wu et al. 2005) if the observation frequency ν is less than the

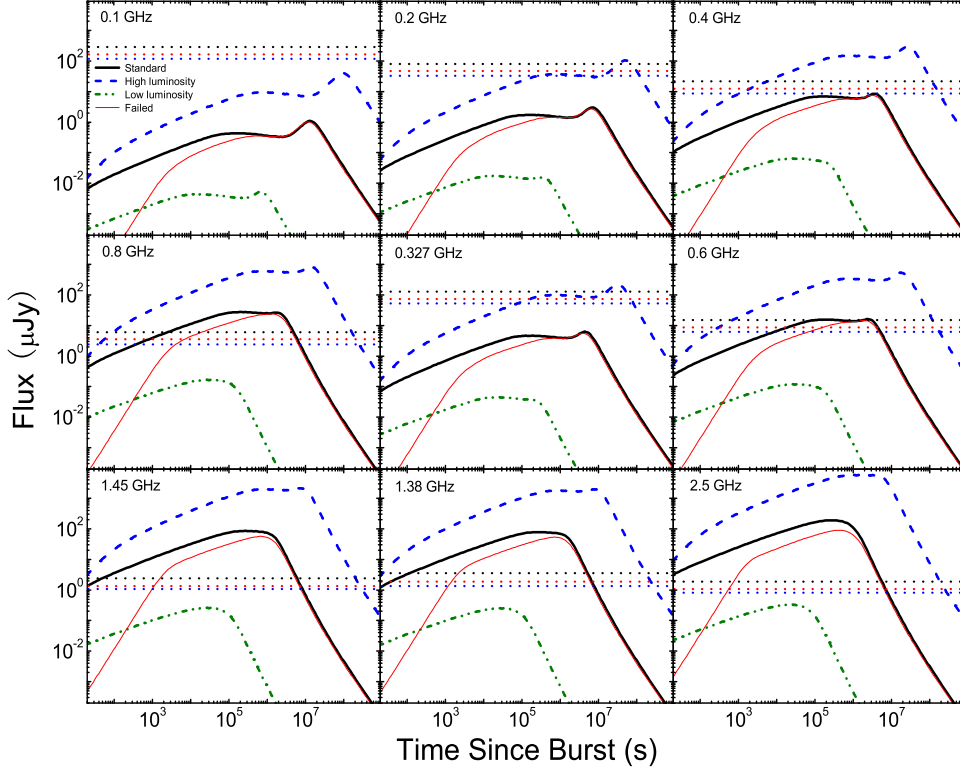


Fig. 1 Radio flux density of GRBs at a redshift $z = 0.5$ versus observation time t in the observer frame at various frequencies within the FAST’s window. The radio light curves of standard, high-luminosity, low-luminosity and failed GRBs are marked with thick solid, dashed, dash-dot-dot and thin solid lines, respectively, and have been symbolized in panel 1. Three horizontal dotted lines from upper to bottom represent 1σ limiting flux density of the FAST for 10, 30 and 60 minutes integration time correspondingly. See the text for details.

$\Delta = 100$ MHz and the aperture efficiency as $\eta_A = 0.65$ for FAST, we have plotted the 1σ and 3σ limiting flux density for a 10-minute integration time for comparison (see Fig. 6).

We can see from Panel (a) in Fig. 6 that radio afterglows of failed bursts are detectable only for nearby sources with redshifts less than 5 and at relatively high frequencies. Panel (b) shows that the radio peaks of low luminosity bursts are far below the detection limits in all our cases and thus are difficult to detect by FAST. On the contrary, we see from Panel (c) that the peak flux densities of high luminosity GRBs are always above the detection limits, making them be the best candidates for monitoring at almost any redshifts and frequencies except very high redshift at lower frequency of $\nu < 200$ MHz. Panel (d) displays the radio peaks of the standard GRBs. They can be observed by FAST up to very high redshift of $z = 10$ at higher frequency, very different from the failed bursts with relatively lower flux density at higher frequency, although they exhibit similar observational properties at lower redshifts in all the frequency bands of FAST. Another

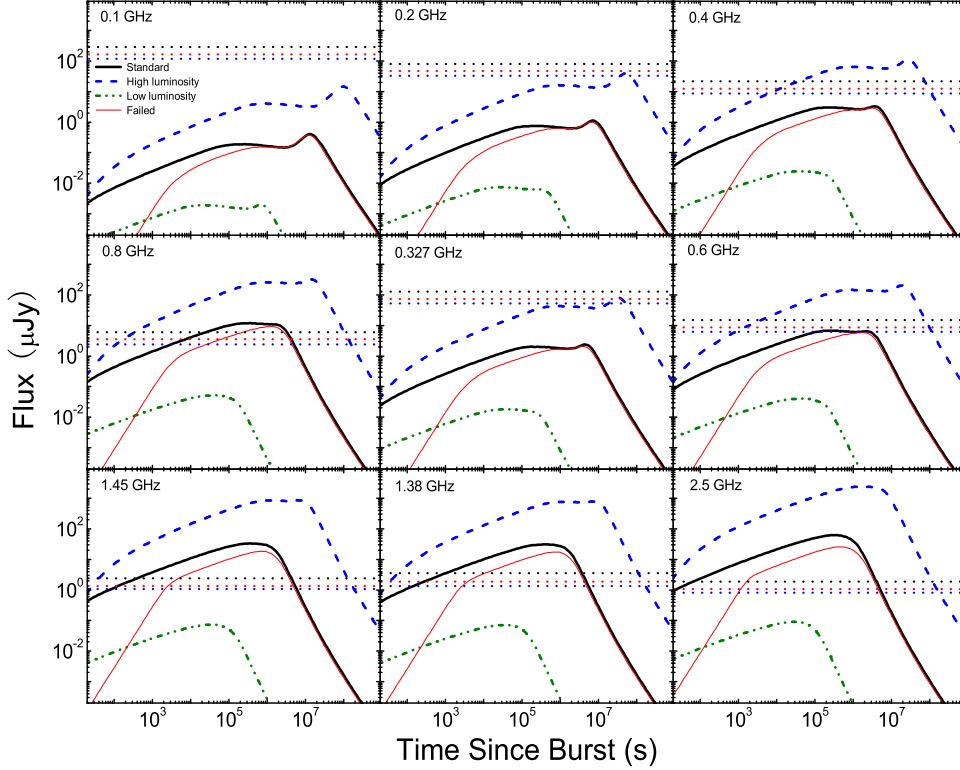


Fig. 2 Radio flux density of GRBs at a redshift $z = 1$ versus observation time t in the observer frame at various frequencies within the FAST’s window. Symbols are the same as in Fig. 1.

In addition, the spectral shape of low luminosity bursts clearly differs from that of other classes of GRBs which hints they may be of distinct physical origin.

5 CONCLUSION AND DISCUSSION

We summarize our major conclusions in the following. Firstly, we presented a quantitative prediction for the detection possibility of GRB radio afterglows with FAST, based on the generic dynamical afterglow model. Our calculations are carried out for four kinds of bursts, i.e. failed GRBs, low luminosity GRBs, high luminosity GRBs and standard GRBs. We found that the radio afterglow detection rate sensitively depends on the model parameters of Lorentz factor and isotropic energy. Secondly, we predicted that radio afterglows of all the above types of bursts except the low luminosity ones should be detected by FAST in rather wide ranges of time, frequency and redshift. The detection possibilities are in degression order for high luminosity, standard, failed and low luminosity GRBs, respectively. Thirdly, FAST is able to detect radio afterglows of GRBs at redshift up to $z \sim 10$ or even more, which will be very helpful for the studies of GRB event rate and GRB cosmology. Considering that GRBs with $E_{iso} = 10^{51} - 10^{53}$ erg at $z \geq 20$ will be observed by the next generation instruments in near infrared and radio bands (Mesler et al. 2014), our results would be very valuable for making further survey plans of GRB radio afterglows with the upcoming

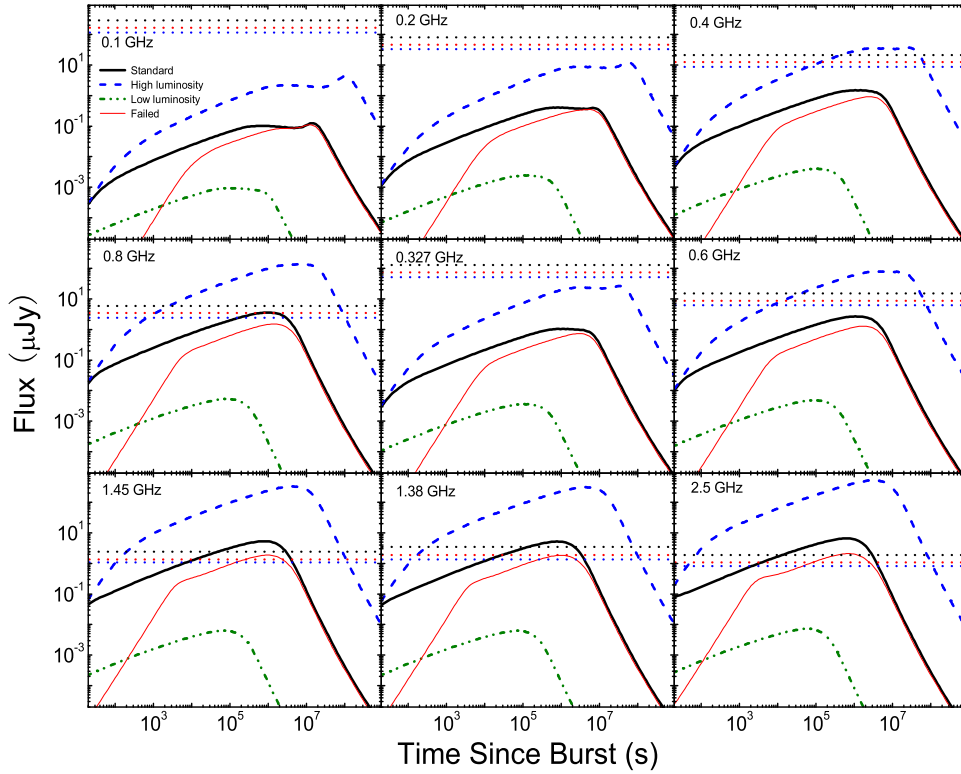


Fig. 3 Radio flux density of GRBs at a redshift $z = 5$ versus observation time t in the observer frame at various frequencies within the FAST's window. Symbols are the same as in Fig. 1.

It is interesting to note that the fractions of high, low and medium isotropic energy GRBs in the pre-Swift era are 4%, 16% and 80% respectively (Friedman & Bloom 2005). As Swift/BAT is more sensitive to long-soft bursts than pre-Swift missions, the percentages are 32%, 3% and 65% respectively for the high, low and medium isotropic energy GRBs in the Swift era. Obviously, the fraction of high luminosity GRBs detected by Swift/BAT is much larger than that of pre-Swift detectors, while the fraction of low luminosity GRBs is just the opposite. The on-going Swift satellite favors long bursts with higher redshifts on average. It will promote the study of early cosmology especially with the help of future FAST observations. This advantage is mainly attributed to the fact that long GRBs with high-redshifts are generally thought to be produced by higher luminosity sources, e.g. collapse of very massive stars.

Rhoads (1997) had pointed out that γ -ray radiation from jetted GRBs can not be observed owing to relativistic beaming effects, but the corresponding late time afterglow emission is less beamed and can safely reach us. These lower frequency radiations are called as orphan afterglows, since they are not associated with any detectable GRBs. However, Huang, Dai & Lu (2002) pointed out another possibility that orphan afterglows can also be produced by failed GRBs (or a dirty fireballs). They argued that the number of failed GRBs may be much larger than that of normal bursts. It is very difficult to distinguish the two different origins of orphan afterglows. The initial Lorentz factor of ejecta is a key parameter that makes the failed

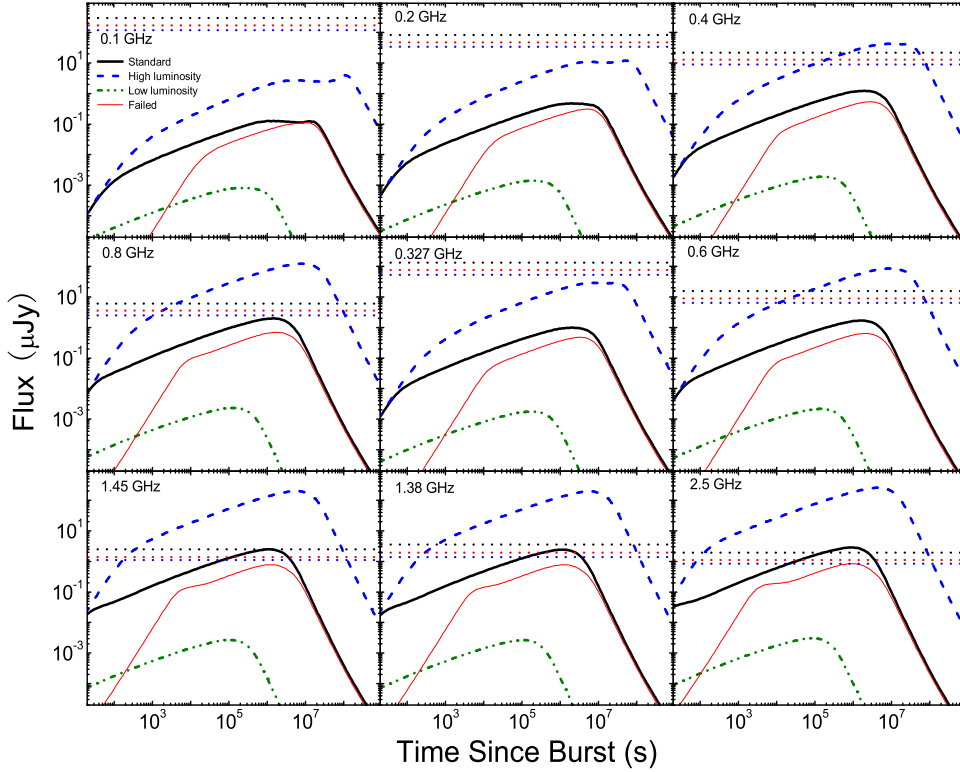


Fig. 4 Radio flux density of GRBs at a redshift $z = 10$ versus observation time t in the observer frame at various frequencies within the FAST’s window. Symbols are the same as in Fig. 1.

method for estimating the initial Lorentz factor (Zou, Fan & Piran 2011). Unfortunately, current Lorentz factor estimates are still controversial although extensive attempts had been made both theoretically and observationally (e.g. Li 2010; Liang et al. 2010, 2011; Zou & Piran 2010; Zou, Fan & Piran 2011; Zhao, Li & Bai 2011; Chang et al. 2012; Hascoet et al. 2013). It is helpful that one can discriminate between failed and standard GRBs from their radio afterglows because such low frequency emission can be observed for quite a long time (Huang, Dai & Lu 2002).

Note that contributions of host galaxies to radio fluxes have been neglected in our numerical calculations for simplification. This effect will add difficulties for afterglow observations with FAST and the detection rate of radio afterglows maybe less optimistic than our current study (Li et al. 2014). On the other hand, the system temperature T_{sys} is sensitively dependent on a variety of realistic factors and will be measured only after the radio telescope is built. As a single dish antenna, FAST will operate in a lower frequency range, i.e. from 70 MHz to 3 GHz in its first phase, and may extend to 8GHz in its second phase. The Low Frequency Array (LOFAR) covers relatively lower observation frequencies of 10-240 MHz (van Haarlem et al. 2013), partly overlapped with that of FAST. Thompson et al. (2007) gave the theoretical equation, $T_{sky} = 60\lambda^{2.55}$ K, as the estimation of T_{sys} . It is illustrated that the LOFAR will be sky-noise dominated under 65 MHz, close to the FAST’s lower frequency limit of 70 MHz. In contrast, at a frequency of 200

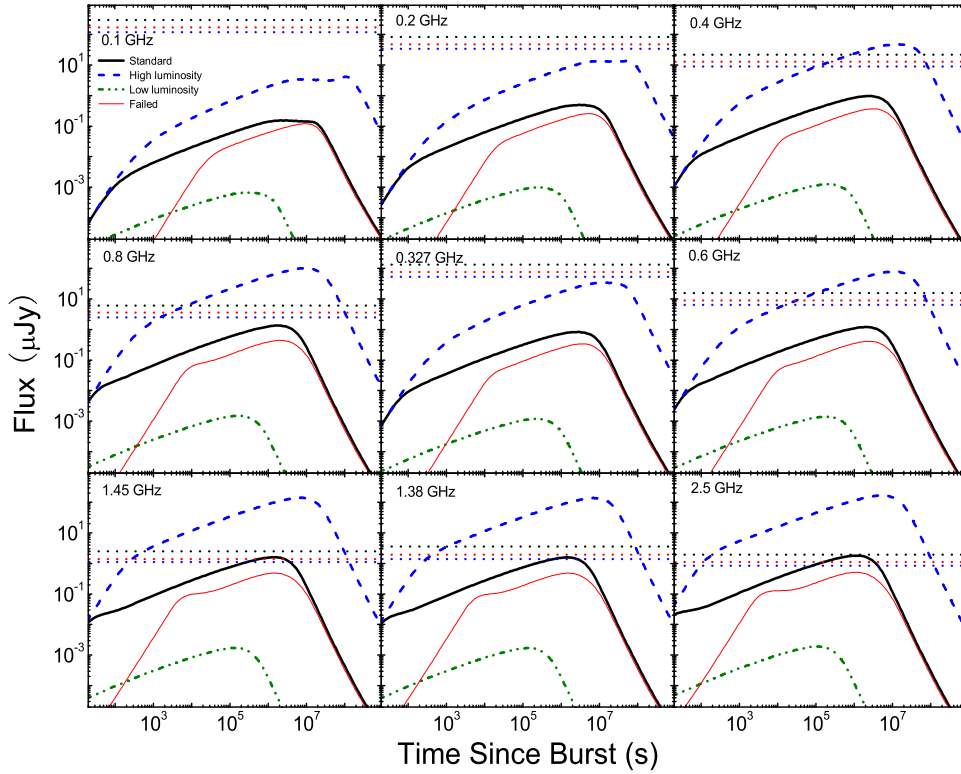


Fig. 5 Radio flux density of GRBs at a redshift $z = 15$ versus observation time t in the observer frame at various frequencies within the FAST's window. Symbols are the same as in Fig. 1.

stress that the limiting sensitivity of FAST at $\nu > 0.4$ GHz for 1-hour integration time is under $10 \mu\text{Jy}$, which is much better than EVLA if FAST's instrumental noise is ideally controlled to be below the values adopted in this work. In this case, we deduce that FAST will be the most powerful new-generation radio telescope for studying radio afterglows. If the international Very-Long-Baseline Interferometry operation is applied, FAST would have more powerful capability of detecting radio emission from low luminosity GRBs or very distant (Chandra et al. 2010) GRBs, which should largely increase the detection rate of radio afterglows in the near future.

Acknowledgements We acknowledge R. D. Nan, B. Zhang, X. F. Wu, Y. Z. Fan, C. S. Choi and H. Y. Chang for helpful discussions. This work was supported by the National Basic Research Program of China (973 Program, Grant No. 2014CB845800) and the National Natural Science Foundation of China (Grant No. 11033002; 11263002). SWK acknowledges support by China Postdoctoral science foundation under grant 2012M520382.

References

Blandford, R. D. & McKee, C. F. 1976, Phys. Fluids, 19, 1130

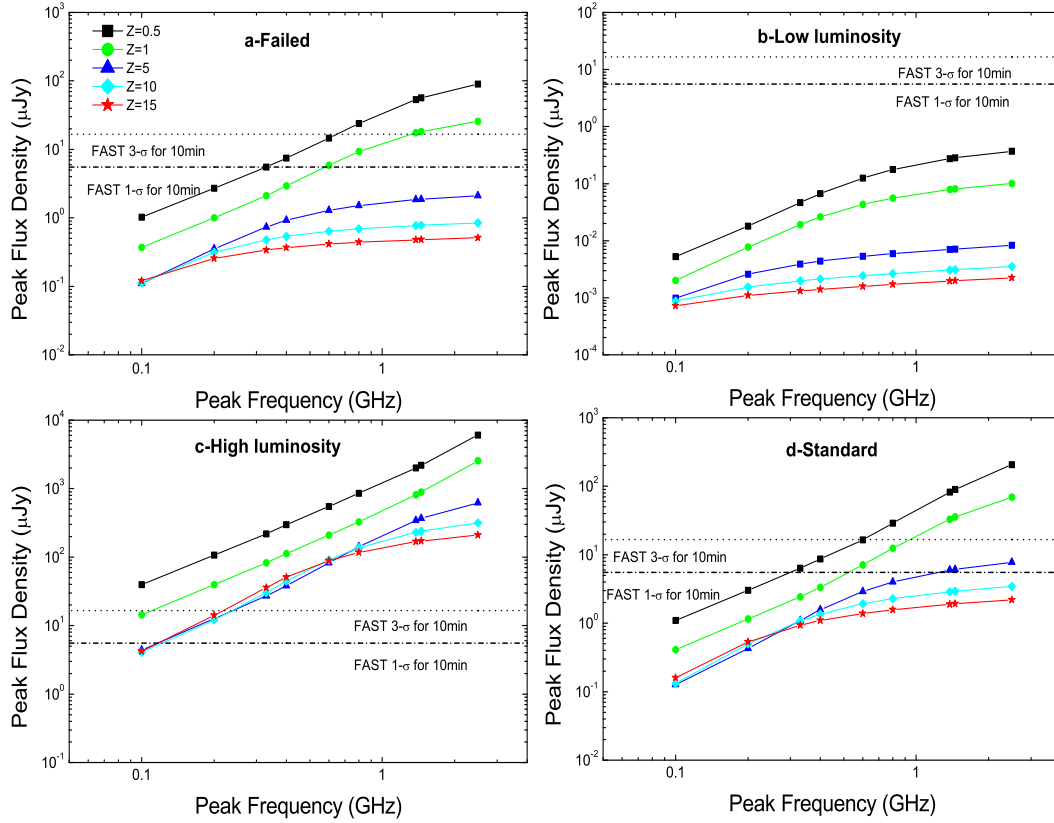


Fig. 6 Peak radio flux density versus peak frequency for the failed, low luminosity, high luminosity and standard GRBs at five representative redshifts. The two horizontal lines from top to bottom respectively stand for 3σ and 1σ limiting flux density of FAST in a 10-minute integration time. The different symbols for various redshifts are given in the first panel. Note that a systematic temperature of $T_{sys}=20\text{K}$ and a bandwidth of $\Delta\nu=100\text{ MHz}$ as typical parameters for FAST have been used for our estimation here. See the text for details.

Chandra, P., Frail, D. A., Fox, D., et al., 2010, *ApJ*, 712, 31

Chang, Z., Lin, H. N., Jiang, Y.G., 2012, *ApJ*, 759, 129

Ciardi, B. & Loeb, A. 2000, *ApJ*, 540, 687

Frail, D. A., Cameron, P. B., Kasliwal, M., et al. 2006, *ApJ*, 646, L99

Friedman, A. S. & Bloom, J. S., 2005, *ApJ*, 627, 1

Gehrels, N., Barthelmy, S. D., Burrows, D. N., et al. 2008, *ApJ*, 689, 1161

Gehrels, N. & Razzaque, S., *Frontiers of Physics*, submitted, arXiv:1301.0840

Ghirlanda, G., Salvaterra, R., Burlon, D. et al., 2013, arXiv:1307.7704

Gou, L. J., Mészáros, P., Abel, T., Zhang, B., 2004, *ApJ*, 604, 508

Hascoet, R., Beloborodov, A. M., Daigne, F., Mochkovitch, R., 2013, arXiv:1304.5813

- Huang, Y. F., Dai, Z. G., & Lu, T. 2000a, MNRAS, 316, 943
- Huang, Y. F., Gou, L. J., Dai, Z. G., Lu, T. 2000, ApJ, 543, 90
- Huang, Y. F., Dai, Z. G., Lu, T. 2000c, A&A, 355, L43
- Huang, Y. F., Dai, Z. G., Lu, T. 2002, MNRAS, 332, 735
- Huang, Y. F., Cheng, K. S. 2003, MNRAS, 341, 63
- Huang, Y. F., Wu, X. F., Dai, Z. G. et al. 2004, ApJ, 605, 300
- Kann, D. A., Klose, S., Zhang, B., et al. 2011, ApJ, 734, 96
- Kong, S. W., Huang, Y. F., Cheng, K. S., Lu, T., 2009, Sci. China Ser. G., 52, 2047
- Kong, S. W., Wong, A. Y. L., Huang, Y. F., Cheng, K. S., 2010, MNRAS, 402, 409
- Li, L. B., Huang, Y. F., Zhang Z. B., et al., 2014, in preparation
- Li, Z., 2010, ApJ, 709, 525
- Liang, E. W., Yi, S. X., Zhang, J., et al., 2010, ApJ, 725, 2209
- Liang, E. W., Lü, H. J., Yi, S. X., Zhang, B., Zhang, B. B., 2011, IJMPD, 20, 1955
- Lu, T., Huang, Y. F., Dai, Z. G., Wei, D. M. 2004, ASSL, 304, 225
- Mesler, R. A., Whalen, D. J., Smidt, J., et al., 2014, Arxiv: 1401.5565
- Nan R. D., Li D., Jin C. J., et al., 2011, IJMPD, 20, 989
- Nysewander, M., Fruchter, A. S., & Peer, A. 2009, ApJ, 701, 824
- Piran, T., 2004, RvMP, 76, 1143
- Postigo, A. de Ugarte, Lundgren, A., Martin, S. et al., 2012, A&A, 538, 44
- Sakamoto, T., Barthelmy, S. D., Baumgartner, W. H., et al. 2011, ApJS, 195, 2
- Sari, R., Piran, T. & Narayan, R., 1998, ApJL, 497, 17
- Salvaterra R., Campana S., Vergani S. D., et al., 2012, ApJ, 749, 68
- Sedov, L. 1969, Similarity and Dimensional Methods in Mechanics, Chap. 4 (New York: Academic)
- Staley, T. D., Titterington, D. J., Fender, R. P. et al., 2013, MNRAS, 428, 3114
- Wang, X., Huang, Y. F., Kong, S. W. 2009, A&A, 505, 1213
- Xu, M., Huang, Y. F., 2010, A&A, 523, 5
- Yu, Y. B., Huang, Y. F., 2013, RAA, 13, 662
- Yue, N. N., Li, D., Zhao, G. B., 2013, in preparation.
- van Haarlem, M. P., Wise, M. W., Gunst, A. W. et al., 2013, A&A, 556, 53
- Wu, X. F., Dai, Z. G., Huang, Y. F., Lu, T., 2005, ApJ, 619, 968
- Zhang B., 2007, ChJAA, 7, 1
- Zhao, X. H., Li, Z., Bai, J. M., 2011, ApJ, 726, 89
- Zou, Y. C. & Piran, T., 2010, MNRAS, 402, 1854
- Zou, Y. C., Fan, Y. Z., Piran, T., 2011, ApJ, 726, L2